

A Novel Wideband MIMO Car-to-Car Channel Model Based on a Geometrical Semi-Circular Tunnel Scattering Model

Nurilla Avazov and Matthias Pätzold

Faculty of Engineering and Science, University of Agder

P.O. Box 509, NO-4898 Grimstad, Norway

E-mails: {nurilla.k.avazov, matthias.paetzold}@uia.no

Abstract — In this paper, we present a wideband multiple-input multiple-output (MIMO) car-to-car (C2C) channel model based on a geometrical semi-circular tunnel (SCT) scattering model. From the geometrical SCT scattering model, a reference channel model is derived under the assumption of single-bounce scattering in line-of-sight (LOS) and non-LOS (NLOS) propagation environments. In the proposed reference channel model, it is assumed that an infinite number of scatterers are randomly distributed on the tunnel wall. Starting from the geometrical scattering model, the time-variant transfer function (TVTF) is derived, and its correlation properties in time, frequency, and space are studied. Expressions are presented for the space-time-frequency cross-correlation function (STF-CCF), the two-dimensional (2D) space CCF, the 2D time-frequency CCF (TF-CCF), the temporal autocorrelation function (ACF), and the frequency correlation function (FCF). Owing to the semi-circular geometry, we reduced the originally threefold integrals to double integrals in the computations of the correlation functions, which simplifies the numerical analysis considerably. From the TVTF characterizing the reference model, an efficient sum-of-cisoids (SOC) channel simulator is derived. Numerical results show that both the temporal ACF and the FCF of the SOC channel simulator match very well with those of the reference model. A validation of the proposed model has been done by fitting the delay spread of the reference model to that of the measured channel, which demonstrates an excellent agreement. The proposed channel simulator allows us to evaluate the performance of C2C communication systems in tunnel environments.

Index Terms — Angle-of-arrival (AOA), angle-of-departure (AOD), car-to-car (C2C), delay spread, diffuse component, frequency correlation function (FCF), line-of-sight (LOS) component, semi-circular tunnel (SCT) scattering model, time-variant transfer function (TVTF).

I. INTRODUCTION

In recent years, there has been an increased interest in developing car-to-car (C2C) communication systems that offer new traffic telematic applications for improving safety and mobility on roads. Efficient C2C communication systems integrate information and communication technology into transport infrastructures, cars, and end-user devices [1]. To improve safety in C2C communication environments, many research projects have been carried out throughout the world, for example, the C2C Communication Consortium [2], the European Road Transport Telematics Implementation Coordinating Organization (ERTICO) [3] in Europe and the Intelligent Transportation Systems (ITS) [4] in the United States. Despite many research and technological development activities, C2C communication systems still face some challenges, induced by safety requirements and wireless channel conditions. One of the most important issues in C2C communications is the channel congestion, causing the loss of safety messages [5].

To achieve the best performance of future C2C communication systems, it is important to have a detailed knowledge of the statistical properties of the underlying radio channel. Numerous mobile-to-mobile (M2M) channel models have been developed based on different geometrical scattering models, such as the two-ring model [6], the elliptical model [7], the rectangular model [8], the T-junction model [9], the cross-junction model [10], and the curve model [11]. Narrowband multiple-input multiple-output (MIMO) C2C channel models can be found in [12, 13] for 5.9 GHz, which is the carrier frequency in dedicated short-range communication (DSRC) [14] systems. However, all these models are 2D models, which have been proposed for certain environments, such as suburban and rural areas. To provide more appropriate radio propagation models for urban areas, three-dimensional (3D) MIMO M2M channel models have been developed and studied in [15–17]. A 3D geometrical scattering model based on concentric spheres at the transmitter and the receiver is assumed in [16, 17]. In [17], a 3D parametric reference model for 2×2 M2M wideband dual-polarized multipath fading channels has been developed. In [18], the importance of different propagation mechanisms in non-line-of-sight (NLOS) propagation conditions are highlighted for merging lanes on highways and four-way cross-junction scenarios. For vehicle-to-vehicle (V2V) communications, new wideband single-input single-output (SISO) and MIMO channel models based on measurement campaigns carried out at 5.2 GHz have been presented in [19] and [20], respectively.

To characterize propagation channels and to evaluate the performance of wireless communication systems, it is important to distinguish between slow and fast

fading. For example, it is well-known that the Doppler spread can be computed from the temporal autocorrelation function (ACF). The Doppler spread is one of the most important characteristic quantities of C2C channels. In the literature [12, 21–23], several C2C channel measurements have been carried out to investigate the Doppler spread of C2C channels. One advantage of geometry-based stochastic channel models is that their spatial and temporal correlation properties can be studied analytically. Thus, the temporal and spatial correlation properties of C2C channels influence the performance of C2C communication systems [24]. The effect of the temporal and spatial correlation properties of C2C channels on the system performance (bit error probability) of Alamouti-coded orthogonal frequency division multiplexing (OFDM) systems has been studied in [25].

In [19], the geometry-based stochastic model (GBSM) approach [20] has been used to model the discrete scattering component under the assumption that the underlying V2V channel is non-stationary. In general, C2C channels are non-stationary in nature. However, for non-stationary channels, it has been reported in the literature [19, 20, 26] that the wide-sense stationary uncorrelated scattering (WSSUS) assumption is still valid for short observation time intervals, commonly referred to as stationary intervals [27]. The performance of C2C communication systems has recently been studied in [28], where a new regular-shaped GBSM for non-isotropic scattering wideband C2C Rician channels has been proposed.

Roads are often passing through tunnels, which can have different geometrical shapes [29, p. 31], such as rectangular, horseshoe, oval, circular, and semi-circular shapes. Modelling of channels in tunnel environments is of importance for the development of C2C communication systems. It is especially important for countries with mountainous areas, where many roads are passing through tunnels. The characteristics of mobile radio channels inside a tunnel environment have been widely investigated by using a geometrical optical model [30], a wave guide model [31], and a full wave model [32]. A theoretical analysis of the wireless channel in tunnels with vehicular traffic flow has been introduced in [33]. It has been shown that the signal propagation in these tunnels is influenced by the number, size, and position of the vehicles, the size of the tunnel, and the vehicular traffic load. In [34], a ray-tube tracing method has been presented to simulate the wave propagation in curved road tunnels. A parametric study has been carried out to investigate the influence of the tunnel geometry and the carrier frequency on the path loss. A geometrical stochastic channel model for train-to-train communications has been derived based on the WINNER model in [35]. There, it has been shown that the channel statistics of the WINNER-based model are close to the deterministic one, which are obtained

from a 3D ray tracing simulator. In [36], a channel inside an arched tunnel was measured and the radio propagation channel in terms of the delay spread and dominant scatterers was analyzed. The investigations showed that more than 90% of the extracted paths consist of LOS and single-bounce scattering components.

In channel modelling, the distribution of the scatterers is an important aspect affecting the angle-of-departure (AOD) and the angle-of-arrival (AOA) statistics. In 3D scattering models, the knowledge of the distributions of the elevation and azimuth angles of the transmitted and the received plane waves is important, as it allows us to investigate the temporal, frequency, and spatial correlation properties of the underlying fading channel. In this regard, the proposed models for tunnel environments [30–34] do *not* consider the impact of the distributions of the scatterers on the statistics of the azimuth AOD (AAOD), azimuth AOA (AAOA), elevation AOD (EAOD), and the elevation AOA (EAOA). To fill this gap, we have recently proposed a wideband SISO C2C channel model based on a geometrical semi-circular tunnel (SCT) scattering model [37].

In this paper, we expand the channel model proposed in [37] by considering the effect of multiple antennas at both the mobile transmitter and the mobile receiver. In this regard, we derive a wideband MIMO C2C channel model from the geometrical SCT scattering model, in which the effect of LOS and NLOS propagation conditions is taken into account.

To simplify the mathematical analysis, we have assumed that the WSSUS assumption is valid over a short observation time interval. This assumption is supported by the study in [26], where the authors investigated the time interval over which the fading process in a tunnel environment can be considered as wide-sense stationary. The analysis of the measurement data in [26] has revealed that the mean stationary intervals in LOS and LOS delay compensated tunnel scenarios are 0.97 s and 1.6 s, respectively.

We study the statistical characteristics of a wideband reference channel model assuming that an infinite number of scatterers are randomly distributed on the SCT wall. Starting from the geometrical SCT scattering model, we derive the TVTF of the reference model assuming single-bounce scattering. An analytical expression is presented for the space-time-frequency (STF) cross-correlation function (STF-CCF) from which the 2D space CCF, the 2D time-frequency (TF) CCF, the temporal ACF, and the frequency correlation function (FCF) are derived directly. Furthermore, we derive an sum-of-cisoid (SOC) channel simulator from the reference model. For deriving our SOC channel simulator, we have used the L_p -norm method (LPNM) [38, Sec. 5.4.3] to compute the model parameters. According to the study

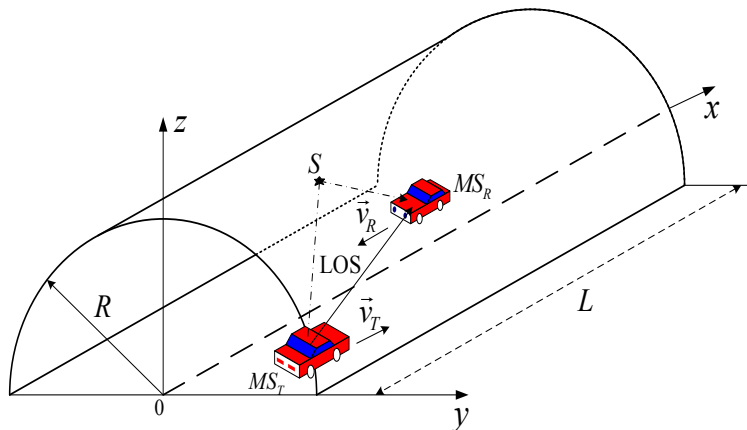


Figure D.1: A typical propagation scenario in an SCT.

in [39], the LPNM has the best performance among the five alternative methods.

It is shown that the designed channel simulator matches closely the underlying reference model with respect to the temporal ACF and the FCF. Finally, we evaluate and present the Doppler statistics and the delay statistics of the proposed SCT channel model. The usefulness of the proposed reference model is validated by demonstrating an excellent match between the delay spread of the reference model and the one of the measured channel reported in [36].

The remainder of this paper is organized as follows. Section II describes the geometrical SCT scattering model. In Section III, the reference channel model is derived from the geometrical SCT scattering model. Section IV analyzes the correlation functions of the reference model, such as the STF-CCF, the 2D space CCF, the 2D TF-CCF, the temporal ACF, and the FCF. In Section V, the simulation model is briefly discussed and a measurement-based computation of the proposed model parameters is presented. The illustration of the numerical results found for the correlation functions characterizing the reference and simulation models is the topic of Section VI. Finally, Section VII provides the conclusion of the paper.

II. THE GEOMETRICAL SCT SCATTERING MODEL

Here, we briefly describe the geometrical SCT scattering model for a wideband MIMO C2C channel. A typical propagation scenario in a tunnel is illustrated in Fig. D.1. The proposed geometrical SCT scattering model describes the scattering environment inside a tunnel with a length of L . It is assumed that the cross-section of the tunnel is a semi-circle with radius R . We assume that the scatterers are randomly distributed on the tunnel wall as shown in Fig. D.2.

The geometrical SCT scattering model is shown in Fig. D.3, where we use the Cartesian coordinate system (x, y, z) to describe the position of the scatterers $S^{(mn)}$

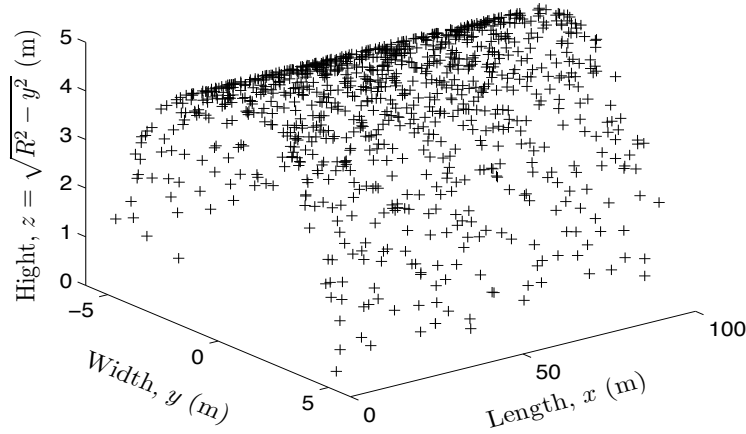


Figure D.2: Randomly distributed scatterers (+) on a tunnel wall with radius $R = 5$ m and length $L = 100$ m.

for $m = 1, 2, \dots, M$ and $n = 1, 2, \dots, N$. Owing to the semi-circular shape of the tunnel, we can describe the z -axis in terms of the y -axis as $z = \sqrt{R^2 - y^2}$. This allows us to present the position of the scatterers $S^{(mn)}$ in the 3D plane by $(x_m, y_n, \sqrt{R^2 - y_n^2})$, where x_m and y_n are random variables. Hence, the distribution of the scatterers $S^{(mn)}$ is completely determined by the distribution of x_m and y_n .

The symbols MS_T and MS_R in Fig. D.3 stand for the mobile transmitter and the mobile receiver, respectively. We assume that the mobile transmitter (receiver) is equipped with a uniform linear antenna array consisting of M_T (M_R) antenna elements. The spacings between the antenna elements at the transmitter and the receiver antennas are denoted by δ_T and δ_R , respectively. The orientations of the

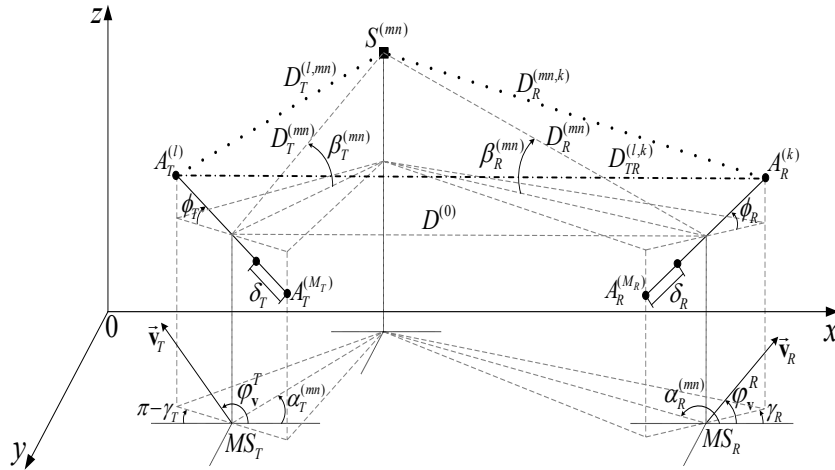


Figure D.3: Geometrical SCT scattering model with single-bounce components (\cdots) and a LOS component ($- \cdot -$) for an $M_T \times M_R$ MIMO C2C channel.

transmitter and the receiver antenna elements in the xy -plane relative to the x -axis

are described by the angles γ_T and γ_R , respectively. Similarly, the elevation angles of the transmitter and the receiver antenna arrays with respect to the xy -plane are denoted by ϕ_T and ϕ_R , respectively. The positions of the antenna arrays of the mobile transmitter MS_T and the mobile receiver MS_R are determined by (x_T, y_T, z_T) and (x_R, y_R, z_R) , respectively. It is supposed that the mobile transmitter MS_T and the mobile receiver MS_R are inside the tunnel, such that $0 \leq x_T \leq x_R \leq L$ and $-R < y_T \leq y_R < R$. It is assumed that there is a LOS path between the mobile transmitter and the mobile receiver. The angles $\alpha_T^{(mn)}$, $\alpha_R^{(mn)}$, $\beta_T^{(mn)}$, and $\beta_R^{(mn)}$ denote the AAOD, AAOA, EAOD, and the EAOA, respectively. Moreover, it is assumed that both the transmitter and the receiver move with speeds v_T and v_R in the direction determined by the angles of motion φ_V^T and φ_V^R , respectively. The distance $D_T^{(l,mn)}$ denotes the path length between the l th transmitter antenna $A_T^{(l)}$ ($l = 1, 2, \dots, M_T$) and the scatterer $S^{(mn)}$, whereas $D_R^{(mn,k)}$ is the distance from the scatterer $S^{(mn)}$ to the k th receiver antenna $A_R^{(k)}$ ($k = 1, 2, \dots, M_R$). Finally, the symbol $D_{TR}^{(l,k)}$ denotes the length of the LOS path from the l th transmitter antenna to the k th receiver antenna. In our analysis, we assume single-bounce scattering and consider the scattering effects only from the scatterers which are located between the transmitter and receiver. These scatterers are addressed as *effective scatterers*.

III. REFERENCE MODEL

Here, we present the reference model for the MIMO C2C channel under LOS and NLOS propagation conditions. From the geometrical SCT scattering model the TVTF will be derived and presented as a sum of diffuse, LOS, and specular components.

A. The TVTF

The propagation environment inside the tunnel is characterized by 3D scattering, where $M \cdot N$ effective scatterers $S^{(mn)}$ are randomly distributed on the tunnel wall. The reference model is based on the assumption that the number of local scatterers on the tunnel wall is infinite, i.e., $M, N \rightarrow \infty$. The MIMO C2C channel can be described by an $M_R \times M_T$ channel matrix $\mathbf{H}(\tau', t) = [h_{kl}(\tau', t)]_{M_R \times M_T}$, where $h_{kl}(\tau', t)$ denotes the time-variant impulse response. The time-variant impulse response of the reference model can be expressed as

$$h_{kl}(\tau', t) = h_{kl}^{\text{DIF}}(\tau', t) + h_{kl}^{\text{LOS}}(\tau', t) + h_{kl}^{\text{SPE}}(\tau', t) \quad (\text{D.1})$$

where $h_{kl}^{\text{DIF}}(\tau', t)$, $h_{kl}^{\text{LOS}}(\tau', t)$, and $h_{kl}^{\text{SPE}}(\tau', t)$ denote the impulse responses of the diffuse, LOS, and specular components, respectively.

To further simplify the analysis, we will use the TVTF instead of the impulse response. The TVTF is the Fourier transform of the time-variant impulse response $h_{kl}(\tau', t)$ with respect to the propagation delay τ' , i.e., $H_{kl}(f', t) = \mathcal{F}_{\tau'}\{h_{kl}(\tau', t)\}$ [38, p. 59]. With reference to (D.1), $H_{kl}(f', t)$ can be presented as

$$H_{kl}(f', t) = H_{kl}^{\text{DIF}}(f', t) + H_{kl}^{\text{LOS}}(f', t) + H_{kl}^{\text{SPE}}(f', t) \quad (\text{D.2})$$

where $H_{kl}^{\text{DIF}}(f', t)$, $H_{kl}^{\text{LOS}}(f', t)$, and $H_{kl}^{\text{SPE}}(f', t)$ denote the diffuse, LOS, and specular components of the TVTF, respectively.

From investigations in [40], it is known that single-bounce scattering components carry more energy than double-bounce scattering components. Therefore, in our analysis, we model the diffuse component $H_{kl}^{\text{DIF}}(f', t)$ by only considering the single-bounce scattering effects. From the geometrical SCT scattering model shown in Fig. D.3, we can observe that the (m, n) th homogeneous plane wave emitted from the l th transmitter antenna element $A_T^{(l)}$ travels over the local scatterer $S^{(mn)}$ before impinging on the k th receiver antenna element $A_R^{(k)}$. Hence, the diffuse component $H_{kl}^{\text{DIF}}(f', t)$ of the TVTF of the link from $A_T^{(l)}$ to $A_R^{(k)}$ can be derived as

$$H_{kl}^{\text{DIF}}(f', t) = \lim_{\substack{M \rightarrow \infty \\ N \rightarrow \infty}} \frac{1}{\sqrt{(c_R + 1)MN}} \sum_{m,n=1}^{M,N} e^{-j \frac{2\pi}{\lambda} D_{kl}^{(mn)}} \times e^{j [2\pi f^{(mn)} t + \theta^{(mn)} - 2\pi \tau_{kl}^{(mn)} f']} \quad (\text{D.3})$$

where

$$D_{kl}^{(mn)} = D_T^{(l,mn)} + D_R^{(mn,k)} \quad (\text{D.4})$$

$$f^{(mn)} = f_T^{(mn)} + f_R^{(mn)} \quad (\text{D.5})$$

$$f_T^{(mn)} = f_{T_{\max}} \cos(\alpha_T^{(mn)} - \varphi_V^T) \cos(\beta_T^{(mn)}) \quad (\text{D.6})$$

$$f_R^{(mn)} = f_{R_{\max}} \cos(\alpha_R^{(mn)} - \varphi_V^R) \cos(\beta_R^{(mn)}). \quad (\text{D.7})$$

The symbol $D_{kl}^{(mn)}$ in (D.3) denotes the total distance, which a plane wave travels from the l th transmitter antenna element to the k th receiver antenna element via the scatterer $S^{(mn)}$. The total distance $D_{kl}^{(mn)}$ is determined by (D.4) in which the distances $D_T^{(l,mn)}$ and $D_R^{(mn,k)}$ are given by

$$D_T^{(l,mn)} = D_T^{(mn)} - (M_T - 2l + 1) \frac{\delta_T}{2} \left[\cos \phi_T \cos(\beta_T^{(mn)}) \cos(\gamma_T - \alpha_T^{(mn)}) + \sin \phi_T \sin(\beta_T^{(mn)}) \right] \quad (\text{D.8})$$

$$D_R^{(mn,k)} = D_R^{(mn)} - (M_R - 2k + 1) \frac{\delta_R}{2} \left[\cos \phi_R \cos \left(\beta_R^{(mn)} \right) \cos \left(\gamma_R - \alpha_R^{(mn)} \right) + \sin \phi_R \sin \left(\beta_R^{(mn)} \right) \right] \quad (\text{D.9})$$

respectively, where

$$D_T^{(mn)} = \left[(x_m - x_T)^2 + (y_n - y_T)^2 + (\sqrt{R^2 - y_n^2} - z_T)^2 \right]^{\frac{1}{2}} \quad (\text{D.10})$$

$$D_R^{(mn)} = \left[(x_m - x_R)^2 + (y_n - y_R)^2 + (\sqrt{R^2 - y_n^2} - z_R)^2 \right]^{\frac{1}{2}}. \quad (\text{D.11})$$

In (D.6) and (D.7), the symbols $f_{T_{\max}} = v_T/\lambda$ and $f_{R_{\max}} = v_R/\lambda$ denote the maximum Doppler frequencies associated with the transmitter and the receiver, respectively, where λ is the wavelength. The symbol c_R in (D.3) is the summation of the Rice factors c_R^{LOS} and c_R^{SPE} , i.e., $c_R = c_R^{\text{LOS}} + c_R^{\text{SPE}}$. The Rice factors c_R^{LOS} and c_R^{SPE} will be defined in the paragraphs after (D.17) and (D.23), respectively. The phase $\theta^{(mn)}$ in (D.3) denotes the phase shift caused by the interaction of the transmitted plane wave and the effective scatterers $S^{(mn)}$. It is assumed that the phases $\theta^{(mn)}$ are independent, identically distributed (i.i.d.) random variables, which are uniformly distributed over the interval $[0, 2\pi)$. Finally, the symbol $\tau_{kl}^{(mn)}$ in (D.3) denotes the propagation delay of the diffuse component. Using $D_{kl}^{(mn)}$ in (D.4), the propagation delays $\tau_{kl}^{(mn)}$ can be computed as $\tau_{kl}^{(mn)} = D_{kl}^{(mn)}/c_0$, where c_0 is the speed of light. It is worth mentioning that one can easily extend our analysis on the basis of single-bounce scattering to the case of double-bounce scattering by following a similar approach as in [11].

In an analogous manner, the LOS component $H_{kl}^{\text{LOS}}(f', t)$ of the TVTF can be written as

$$H_{kl}^{\text{LOS}}(f', t) = \sqrt{\frac{c_R^{\text{LOS}}}{c_R + 1}} e^{-j \frac{2\pi}{\lambda} D_{TR, \text{LOS}}^{(l,k)}} e^{j 2\pi [f^{(0)} t - \tau_{kl}^{(0)} f']} \quad (\text{D.12})$$

where

$$D_{TR, \text{LOS}}^{(l,k)} = D^{(0)} - (M_T - 2l + 1) \frac{\delta_T}{2} \cos \phi_T \cos \gamma_T - (M_R - 2k + 1) \frac{\delta_R}{2} \cos \phi_R \cos \left(\alpha_T^{(0)} - \gamma_R \right) \quad (\text{D.13})$$

$$D^{(0)} = \left[(x_R - x_T)^2 + (y_R - y_T)^2 + (z_R - z_T)^2 \right]^{\frac{1}{2}} \quad (\text{D.14})$$

$$f^{(0)} = f_T^{(0)} + f_R^{(0)} \quad (\text{D.15})$$

$$f_T^{(0)} = f_{T_{\max}} \cos(\alpha_T^{(0)} - \phi_v^T) \cos(\beta_T^{(0)}) \quad (\text{D.16})$$

$$f_R^{(0)} = f_{R_{\max}} \cos(\alpha_R^{(0)} - \phi_v^R) \cos(\beta_R^{(0)}). \quad (\text{D.17})$$

In (D.15), $f_T^{(0)}$ and $f_R^{(0)}$ denote the Doppler shifts of the LOS component caused by the movement of the transmitter and the receiver, respectively. The angles $\alpha_T^{(0)}$ ($\beta_T^{(0)}$) and $\alpha_R^{(0)}$ ($\beta_R^{(0)}$) in (D.16) and (D.17) represent the AAOD (EAOD) and the AAOA (EAOA) of the LOS component, respectively. The symbol c_R^{LOS} in (D.12) represents the Rice factor, which is defined as the ratio of the mean power of the LOS component to the mean power of the diffuse component, i.e., $c_R^{\text{LOS}} = E\{|H_{kl}^{\text{LOS}}(f', t)|^2\} / E\{|H_{kl}^{\text{DIF}}(f', t)|^2\}$. In (D.12), the symbol $\tau_{kl}'^{(0)}$ stands for the propagation delay of the LOS component. This quantity is given by $\tau_{kl}'^{(0)} = D_{TR}^{(l,k)} / c_0$.

Similarly to the LOS component, the specular component $H_{kl}^{\text{SPE}}(f', t)$ of the TVTF $H_{kl}(f', t)$ in (D.2) can be presented as

$$H_{kl}^{\text{SPE}}(f', t) = \sqrt{\frac{c_R^{\text{SPE}}}{c_R + 1}} e^{-j\frac{2\pi}{\lambda} D_{TR, \text{SPE}}^{(l,k)}} e^{j2\pi [f^{(1)}t - \tau_{kl}'^{(1)} f']} \quad (\text{D.18})$$

where

$$\begin{aligned} D_{TR, \text{SPE}}^{(l,k)} = & D^{(1)} - (M_T - 2l + 1) \frac{\delta_T}{2} \cos \phi_T \cos \gamma_T \\ & - (M_R - 2k + 1) \frac{\delta_R}{2} \cos \phi_R \cos(\alpha_T^{(1)} - \gamma_R) \end{aligned} \quad (\text{D.19})$$

$$\begin{aligned} D^{(1)} = & \left[(x_s - x_T)^2 + (y_s - y_T)^2 + (\sqrt{R^2 - y_n^2} - z_s)^2 \right]^{\frac{1}{2}} \\ & + \left[(x_s - x_R)^2 + (y_s - y_R)^2 + (\sqrt{R^2 - y_n^2} - z_s)^2 \right]^{\frac{1}{2}} \end{aligned} \quad (\text{D.20})$$

$$f^{(1)} = f_T^{(1)} + f_R^{(1)} \quad (\text{D.21})$$

$$f_T^{(1)} = f_{T_{\max}} \cos(\alpha_T^{(1)} - \phi_v^T) \cos(\beta_T^{(1)}) \quad (\text{D.22})$$

$$f_R^{(1)} = f_{R_{\max}} \cos(\alpha_R^{(1)} - \phi_v^R) \cos(\beta_R^{(1)}). \quad (\text{D.23})$$

The symbol c_R^{SPE} in (D.18) represents the Rice factor, which is defined as the ratio of the mean power of the specular component to the mean power of the diffuse

component, i.e., $c_R^{\text{SPE}} = E\{|H_{kl}^{\text{SPE}}(f', t)|^2\}/E\{|H_{kl}^{\text{DIF}}(f', t)|^2\}$. The symbol $D_{TR, \text{SPE}}^{(l, k)}$ in (D.18) denotes the travelling distance of the plane wave from the l th transmitter antenna element to the k th receiver antenna element via the specular reflection point $S^{(1)}$. The position of the specular reflection point $S^{(1)}$ is determined by (x_s, y_s, z_s) . The symbols $f_T^{(1)}$ and $f_R^{(1)}$ in (D.21) denote the Doppler shifts of the specular component. The angles $\alpha_T^{(1)}$ ($\beta_T^{(1)}$) and $\alpha_R^{(1)}$ ($\beta_R^{(1)}$) in (D.22) and (D.23) represent the AAOD (EAOD) and the AAOA (EAOA) of the specular component, respectively. The symbol $\tau_{kl}'^{(1)}$ in (D.18) stands for the propagation delay of the specular component, which is given by $\tau_{kl}'^{(1)} = D_{TR, \text{SPE}}^{(l, k)}/c_0$. In analogy to [38, p. 61], the LOS component $H_{kl}^{\text{LOS}}(f', t)$ and the specular component $H_{kl}^{\text{SPE}}(f', t)$ of the TVTF are deterministic processes, while the diffuse component $H_{kl}^{\text{DIF}}(f', t)$ is a stochastic process.

B. The Elevation and the Azimuth Angles

In the reference model, the position of all effective scatterers $S^{(mn)}$ is described by the Cartesian coordinates (x_m, y_n) . With reference to Fig. D.3, we take into account that the AAOD $\alpha_T^{(mn)}$ and the AAOA $\alpha_R^{(mn)}$ are dependent. By using trigonometric identities, we can express the AAOD $\alpha_T^{(mn)}$, AAOA $\alpha_R^{(mn)}$, EAOD $\beta_T^{(mn)}$, and EAOA $\beta_R^{(mn)}$ in terms of the coordinates (x_m, y_n) of the position of the scatterers $S^{(mn)}$ as follows:

$$\alpha_i(x_m, y_n) = \begin{cases} f(x_m, y_n), & \text{if } y_n \geq y_i \\ -f(x_m, y_n), & \text{if } y_n < y_i \end{cases} \quad (\text{D.24})$$

$$\beta_i(x_m, y_n) = \begin{cases} -g(x_m, y_n), & \text{if } \sqrt{R^2 - y_n^2} < z_i \\ g(x_m, y_n), & \text{if } \sqrt{R^2 - y_n^2} \geq z_i \end{cases} \quad (\text{D.25})$$

where the index i refers to the transmitter (receiver) if $i = T$ ($i = R$). The functions $f(x, y)$ and $g(x, y)$ are given by

$$f(x_m, y_n) = \arccos\left(\frac{(x_m - x_i)}{\sqrt{(x_m - x_i)^2 + (y_n - y_i)^2}}\right) \quad (\text{D.26})$$

and

$$g(x_m, y_n) = \arccos\left(\frac{\sqrt{(x_m - x_i)^2 + (y_n - y_i)^2}}{\sqrt{(x_m - x_i)^2 + (y_n - y_i)^2 + (\sqrt{R^2 - y_n^2} - z_i)^2}}\right) \quad (\text{D.27})$$

respectively.

IV. CORRELATION PROPERTIES OF THE REFERENCE MODEL

Here, we derive a general analytical solution for the STF-CCF, which will then be used to compute the 2D space CCF, the 2D TF-CCF, the temporal ACF, and the FCF.

A. The STF-CCF

Using (D.2), the STF-CCF between the TVTFs $H_{kl}(f', t)$ and $H_{k'l'}(f', t)$ can be expressed as

$$\begin{aligned} \rho_{kl,k'l'}(\delta_T, \delta_R, \mathbf{v}', \tau) &:= E\{H_{kl}^*(f', t)H_{k'l'}(f' + \mathbf{v}', t + \tau)\} \\ &= \rho_{kl,k'l'}^{\text{DIF}}(\delta_T, \delta_R, \mathbf{v}', \tau) + \rho_{kl,k'l'}^{\text{LOS}}(\delta_T, \delta_R, \mathbf{v}', \tau) \\ &\quad + \rho_{kl,k'l'}^{\text{SPE}}(\delta_T, \delta_R, \mathbf{v}', \tau) \end{aligned} \quad (\text{D.28})$$

where $(*)$ denotes the complex conjugate, and $E\{\cdot\}$ stands for the expectation operator that applies to all random variables: The phases $\theta^{(mn)}$ and the coordinates x_m and y_n defining the position of the scatterers $\mathcal{S}^{(mn)}$.

Using (D.3), the STF-CCF $\rho_{kl,k'l'}^{\text{DIF}}(\delta_T, \delta_R, \mathbf{v}', \tau)$ of the diffuse component $H_{kl}^{\text{DIF}}(f', t)$ can be expressed as

$$\begin{aligned} \rho_{kl,k'l'}^{\text{DIF}}(\delta_T, \delta_R, \mathbf{v}', \tau) &= \lim_{\substack{M \rightarrow \infty \\ N \rightarrow \infty}} \frac{1}{(c_R + 1)MN} \sum_{m,n=1}^{M,N} E \left\{ c_{l'l'}^{(mn)} d_{kk'}^{(mn)} \right. \\ &\quad \left. \times e^{j2\pi \left[f^{(mn)} \tau - \tau_{kl}^{(mn)} \mathbf{v}' \right]} \right\} \end{aligned} \quad (\text{D.29})$$

where

$$\begin{aligned} c_{l'l'}^{(mn)} &= e^{j2\pi \frac{\delta_T}{\lambda} (l-l') \cos \phi_T \cos(\beta_T^{(mn)}) \cos(\gamma_T - \alpha_T^{(mn)})} \\ &\quad \times e^{j2\pi \frac{\delta_T}{\lambda} (l-l') \sin \phi_T \sin(\beta_T^{(mn)})} \end{aligned} \quad (\text{D.30})$$

$$\begin{aligned} d_{kk'}^{(mn)} &= e^{j2\pi \frac{\delta_R}{\lambda} (k-k') \cos \phi_R \cos(\beta_R^{(mn)}) \cos(\gamma_R - \alpha_R^{(mn)})} \\ &\quad \times e^{j2\pi \frac{\delta_R}{\lambda} (k-k') \sin \phi_R \sin(\beta_R^{(mn)})}. \end{aligned} \quad (\text{D.31})$$

The expression above has been obtained by averaging over the random phases $\theta^{(mn)}$. Here, it is important to note that the quantities $c_{l'l'}^{(mn)}$, $d_{kk'}^{(mn)}$, $f^{(mn)}$ and $\tau_{kl}^{(mn)}$ are functions of the coordinates x_m and y_n . The random variables x_m and y_n are supposed to be uniformly i.i.d., such that their probability density functions (PDFs)

are given by [37]

$$p_{x_m}(x) = \frac{1}{(x_R - x_T)}, \quad \text{if } x \in [x_T, x_R] \quad (\text{D.32})$$

$$p_{y_n}(y) = \frac{1}{2R}, \quad \text{if } y \in (-R, R) \quad (\text{D.33})$$

respectively. Hence, the joint PDF $p_{x_m y_n}(x, y)$ of the random variables x_m and y_n can be expressed as the product of the marginal PDFs $p_{x_m}(x)$ and $p_{y_n}(y)$, i.e.,

$$\begin{aligned} p_{x_m y_n}(x, y) &= p_{x_m}(x) \cdot p_{y_n}(y) \\ &= \frac{1}{2R(x_R - x_T)}, \quad \text{if } x \in [x_T, x_R], y \in (-R, R). \end{aligned} \quad (\text{D.34})$$

The infinitesimal power of the diffuse component corresponding to the differential coordinates dx and dy is proportional to $p_{x_m y_n}(x, y) dx dy$. In the limit as $M, N \rightarrow \infty$, this infinitesimal contribution must be equal to $1/(MN)$, i.e., $1/(MN) = p_{x_m y_n}(x, y) dx dy$. Consequently, the STF-CCF $\rho_{kl, k'l'}^{\text{DIF}}(\delta_T, \delta_R, \mathbf{v}', \tau)$ of the diffuse component in (D.29) can be written as

$$\begin{aligned} \rho_{kl, k'l'}^{\text{DIF}}(\delta_T, \delta_R, \mathbf{v}', \tau) &= \frac{1}{2R(x_R - x_T)(c_R + 1)} \int_{-R}^R \int_{x_T}^{x_R} c_{ll'}(x, y) d_{kk'}(x, y) \\ &\quad \times e^{j2\pi[f(x, y)\tau - \tau'_{kl}(x, y)\mathbf{v}']} dx dy \end{aligned} \quad (\text{D.35})$$

where

$$\begin{aligned} c_{ll'}(x, y) &= e^{j2\pi \frac{\delta_T}{\lambda} (l-l') \cos \phi_T \cos(\beta_T(x, y)) \cos(\gamma_T - \alpha_T(x, y))} \\ &\quad \times e^{j2\pi \frac{\delta_T}{\lambda} (l-l') \sin \phi_T \sin(\beta_T(x, y))} \end{aligned} \quad (\text{D.36})$$

$$\begin{aligned} d_{kk'}(x, y) &= e^{j2\pi \frac{\delta_R}{\lambda} (k-k') \cos \phi_R \cos(\beta_R(x, y)) \cos(\gamma_R - \alpha_R(x, y))} \\ &\quad \times e^{j2\pi \frac{\delta_R}{\lambda} (k-k') \sin \phi_R \sin(\beta_R(x, y))} \end{aligned} \quad (\text{D.37})$$

$$f(x, y) = f_T(x, y) + f_R(x, y) \quad (\text{D.38})$$

$$f_T(x, y) = f_{T_{\max}} \cos(\alpha_T(x, y) - \phi_V^T) \cos(\beta_T(x, y)) \quad (\text{D.39})$$

$$f_R(x, y) = f_{R_{\max}} \cos(\alpha_R(x, y) - \phi_V^R) \cos(\beta_R(x, y)) \quad (\text{D.40})$$

$$\tau'_{kl}(x, y) = \frac{1}{c_0} \left(D_T^{(l)}(x, y) + D_R^{(k)}(x, y) \right). \quad (\text{D.41})$$

By using the functions in (D.8) and (D.9), the distances $D_T^{(l)}(x, y)$ and $D_R^{(k)}(x, y)$ in (D.35) can be expressed as

$$D_T^{(l)}(x, y) = D_T(x, y) - (M_T - 2l + 1) \frac{\delta_T}{2} \left[\cos \phi_T \cos(\beta_T(x, y)) \cos(\gamma_T - \alpha_T(x, y)) + \sin \phi_T \sin(\beta_T(x, y)) \right] \quad (D.42)$$

$$D_R^{(k)}(x, y) = D_R(x, y) - (M_R - 2k + 1) \frac{\delta_R}{2} \left[\cos \phi_R \cos(\beta_R(x, y)) \cos(\gamma_R - \alpha_R(x, y)) + \sin \phi_R \sin(\beta_R(x, y)) \right] \quad (D.43)$$

respectively, where

$$D_T(x, y) = \left[(x - x_T)^2 + (y - y_T)^2 + (\sqrt{R^2 - y^2} - z_T)^2 \right]^{\frac{1}{2}} \quad (D.44)$$

$$D_R(x, y) = \left[(x - x_R)^2 + (y - y_R)^2 + (\sqrt{R^2 - y^2} - z_R)^2 \right]^{\frac{1}{2}}. \quad (D.45)$$

In (D.39) and (D.40), we recall that the AAOB (AAOB) $\alpha_T(x, y)$ ($\alpha_R(x, y)$) and the EAOD (EAOD) $\beta_T(x, y)$ ($\beta_R(x, y)$) are functions of the coordinates (x, y) of the scatterers according to (D.24) and (D.25), respectively.

The STF-CCF $\rho_{kl, k'l'}^{\text{LOS}}(\delta_T, \delta_R, \mathbf{v}', \tau)$ of the LOS component can be expressed as

$$\rho_{kl, k'l'}^{\text{LOS}}(\delta_T, \delta_R, \mathbf{v}', \tau) = \frac{c_R}{c_R + 1} c_{ll'}^{(0)} d_{kk'}^{(0)} e^{j2\pi(f^{(0)}\tau - \tau_{kl}^{(0)})\mathbf{v}'} \quad (D.46)$$

where

$$c_{ll'}^{(0)} = e^{j2\pi \frac{\delta_T}{\lambda} (l-l') \cos \phi_T \cos \gamma_T} \quad (D.47)$$

$$d_{kk'}^{(0)} = e^{j2\pi \frac{\delta_R}{\lambda} (k-k') \cos \phi_R \cos(\alpha_R^{(0)} - \gamma_R)}. \quad (D.48)$$

Analogously to the LOS component, the STF-CCF $\rho_{kl, k'l'}^{\text{SPE}}(\delta_T, \delta_R, \mathbf{v}', \tau)$ of the specular component can be presented as

$$\rho_{kl, k'l'}^{\text{SPE}}(\delta_T, \delta_R, \mathbf{v}', \tau) = \frac{c_R^{\text{SPE}}}{c_R + 1} c_{ll'}^{(1)} d_{kk'}^{(1)} e^{j2\pi(f^{(1)}\tau - \tau_{kl}^{(1)})\mathbf{v}'} \quad (D.49)$$

where

$$c_{ll'}^{(1)} = e^{j2\pi \frac{\delta_T}{\lambda} (l-l') \cos \phi_T \cos \gamma_T} \quad (D.50)$$

$$d_{kk'}^{(1)} = e^{j2\pi \frac{\delta_R}{\lambda} (k-k') \cos \phi_R \cos(\alpha_R^{(1)} - \gamma_R)}. \quad (D.51)$$

B. 2D Space CCF

The 2D space CCF $\rho_{kl,k'l'}(\delta_T, \delta_R)$ is defined as $\rho_{kl,k'l'}(\delta_T, \delta_R) := E\{H_{kl}^*(f', t) H_{k'l'}(f', t)\}$, which is equal to the STF-CCF $\rho_{kl,k'l'}(\delta_T, \delta_R, \mathbf{v}', \tau)$ at $\mathbf{v}' = 0$ and $\tau = 0$, i.e., $\rho_{kl,k'l'}(\delta_T, \delta_R) = \rho_{kl,k'l'}(\delta_T, \delta_R, 0, 0)$. Hence, the 2D space CCF can be presented as

$$\begin{aligned} \rho_{kl,k'l'}(\delta_T, \delta_R) &= \frac{1}{2R(x_R - x_T)(c_R + 1)} \int_{-R}^R \int_{x_T}^{x_R} c_{ll'}(x, y) d_{kk'}(x, y) dx dy \\ &\quad + \frac{c_R^{\text{LOS}}}{c_R + 1} c_{ll'}^{(0)} d_{kk'}^{(0)} + \frac{c_R^{\text{SPE}}}{c_R + 1} c_{ll'}^{(1)} d_{kk'}^{(1)}. \end{aligned} \quad (\text{D.52})$$

C. The 2D TF-CCF

The 2D TF-CCF of the reference model is defined as the correlation of the TVTFs $H_{kl}(f', t)$ and $H_{kl}(f', t + \tau)$, i.e., $\rho_{kl}(\mathbf{v}', \tau) := E\{H_{kl}^*(f', t) H_{kl}(f' + \mathbf{v}', t + \tau)\}$. The 2D TF-CCF $\rho_{kl}(\mathbf{v}', \tau)$ can easily be obtained from the STF-CCF $\rho_{kl,k'l'}(\delta_T, \delta_R, \mathbf{v}', \tau)$ by setting the antenna element spacings δ_T and δ_R to zero, i.e., $\rho_{kl}(\mathbf{v}', \tau) = \rho_{kl,k'l'}(0, 0, \mathbf{v}', \tau)$. Thus,

$$\begin{aligned} \rho_{kl}(\mathbf{v}', \tau) &= \frac{1}{2R(x_R - x_T)(c_R + 1)} \int_{-R}^R \int_{x_T}^{x_R} e^{j2\pi(f(x,y)\tau - \tau'_{kl}(x,y)\mathbf{v}')} dx dy \\ &\quad + \frac{c_R^{\text{LOS}}}{c_R + 1} e^{j2\pi(f^{(0)}\tau - \tau'_{kl}^{(0)}\mathbf{v}')} + \frac{c_R^{\text{SPE}}}{c_R + 1} e^{j2\pi(f^{(1)}\tau - \tau'_{kl}^{(1)}\mathbf{v}')} . \end{aligned} \quad (\text{D.53})$$

From the 2D TF-CCF two further correlation functions can be derived, such as the temporal ACF and the FCF.

D. Temporal ACF

The temporal ACF of the TVTF $H(f', t)$ of the transmission link from $A_T^{(l)}$ ($l = 1, 2, \dots, M_T$) to $A_R^{(k)}$ ($k = 1, 2, \dots, M_R$) is defined by $r_{kl}(\tau) := E\{H_{kl}^*(f', t) H_{kl}(f', t + \tau)\}$ [41, p. 376]. Alternatively, the temporal ACF $r_{kl}(\tau)$ can be obtained directly from the 2D TF-CCF $\rho_{kl}(\mathbf{v}', \tau)$ by setting the frequency separation variable \mathbf{v}' to zero, i.e., $r_{kl}(\tau) = \rho_{kl}(0, \tau)$. In both cases, we obtain

$$\begin{aligned} r_{kl}(\tau) &= \frac{1}{2R(x_R - x_T)(c_R + 1)} \int_{-R}^R \int_{x_T}^{x_R} e^{j2\pi f(x,y)\tau} dx dy \\ &\quad + \frac{c_R^{\text{LOS}}}{c_R + 1} e^{j2\pi f^{(0)}\tau} + \frac{c_R^{\text{SPE}}}{c_R + 1} e^{j2\pi f^{(1)}\tau} \end{aligned} \quad (\text{D.54})$$

for $k = 1, 2, \dots, M_R$ and $l = 1, 2, \dots, M_T$. Note that the temporal ACF $r_{kl}(\tau)$ in (D.54) is independent of k and l , which means that all TVTFs $H_{kl}(f', t)$ modelling the link from $A_T^{(l)}$ to $A_R^{(k)}$ are characterized by the same temporal ACF $r_{kl}(\tau)$ for all $k = 1, 2, \dots, M_R$ and $l = 1, 2, \dots, M_T$.

E. The FCF

The FCF of the TVTFs $H_{kl}(f', t)$ and $H_{kl}(f' + \mathbf{v}', t)$ is defined by $r_{kl}(\mathbf{v}') := E\{H_{kl}^*(f', t)H_{kl}(f' + \mathbf{v}', t)\}$ [41, p. 376], which is equal to the 2D TF-CCF $\rho_{kl}(\mathbf{v}', \tau)$ at $\tau = 0$, i.e., $r_{kl}(\mathbf{v}') = \rho_{kl}(\mathbf{v}', 0)$. Thus, the FCF can be written as

$$r_{kl}(\mathbf{v}') = \frac{1}{2R(x_R - x_T)(c_R + 1)} \int_{-R}^R \int_{x_T}^{x_R} e^{-j2\pi\tau'_{kl}(x,y)\mathbf{v}'} dx dy + \frac{c_R^{\text{LOS}}}{c_R + 1} e^{-j2\pi\tau'_{kl}(0)\mathbf{v}'} + \frac{c_R^{\text{SPE}}}{c_R + 1} e^{-j2\pi\tau'_{kl}(1)\mathbf{v}'} . \quad (\text{D.55})$$

In contrast to the temporal ACF $r_{kl}(\tau)$, the FCF $r_{kl}(\mathbf{v}')$ depends on k and l due to the propagation delays $\tau'_{kl}(x, y)$, $\tau'_{kl}(0)$, and $\tau'_{kl}(1)$. However, by assuming that the antenna element spacing of the transmitter (receiver) antenna array δ_T (δ_R) is small in comparison to the radius R of the tunnel arch, we can take profit from the inequality $\max\{\delta_T, \delta_R\} \ll R$. Consequently, the total travelling distance $D_{kl}^{(mn)}$ in (D.4) can be approximated as

$$D_{kl}^{(mn)} \approx D_T^{(mn)} + D_R^{(mn)} \quad (\text{D.56})$$

where $D_T^{(mn)}$ and $D_R^{(mn)}$ are given in (D.10) and (D.11), respectively. Thus, the propagation delays $\tau'_{kl}(x, y)$, $\tau'_{kl}(0)$, and $\tau'_{kl}(1)$ will be independent of k and l .

F. The Doppler power spectral density

The Doppler power spectral density (PSD) is the Fourier transform of the temporal ACF $r_{kl}(\tau)$ with respect to τ , i.e., $S_f(f) = \mathcal{F}_\tau\{r_{kl}(\tau)\}$ [38, Sec. 3.3]. Hence, the Doppler PSD can be presented as

$$S_f(f) = \int_{-\infty}^{\infty} r_{kl}(\tau) e^{-j2\pi f\tau} d\tau . \quad (\text{D.57})$$

The two most important statistical quantities characterizing the Doppler PSD $S_f(f)$ are the *average Doppler shift* $B_f^{(1)}$ and the *Doppler spread* $B_f^{(2)}$ [38, Sec. 3.3]. The average Doppler shift $B_f^{(1)}$ describes the average frequency shift that a carrier frequency experiences during the transmission over a multipath fading channel. The average Doppler shift is defined as the first moment of $S_f(f)$, which can be

expressed as follows

$$B_f^{(1)} = \frac{\int_{-\infty}^{\infty} f S_f(f) df}{\int_{-\infty}^{\infty} S_f(f) df}. \quad (\text{D.58})$$

The Doppler spread $B_f^{(2)}$ describes the frequency spread that a carrier frequency experiences during the transmission over a multipath fading channel. The Doppler spread is defined as the square root of the second central moment of $S_f(f)$, i.e.,

$$B_f^{(2)} = \sqrt{\frac{\int_{-\infty}^{\infty} (f - B_f^{(1)})^2 S_f(f) df}{\int_{-\infty}^{\infty} S_f(f) df}}. \quad (\text{D.59})$$

According to [38, Sec. 3.3], the average Doppler shift $B_f^{(1)}$ and the Doppler spread $B_f^{(2)}$ can alternatively be computed by using Fourier transform techniques enabling to express these quantities in terms of the ACF $r_{kl}(\tau)$ and its first and second time derivatives at the origin as follows:

$$B_f^{(1)} = \frac{1}{2\pi j} \cdot \frac{\dot{r}_{kl}(0)}{r_{kl}(0)} \quad (\text{D.60})$$

$$B_f^{(2)} = \frac{1}{2\pi} \sqrt{\left(\frac{\dot{r}_{kl}(0)}{r_{kl}(0)}\right)^2 - \frac{\ddot{r}_{kl}(0)}{r_{kl}(0)}}. \quad (\text{D.61})$$

G. Power Delay Profile

The power delay profile (PDP) measures the average power associated with a given multipath delay τ'_{kl} . The PDP is the inverse Fourier transform of the FCF with respect to \mathbf{v}' , i.e., $S_{\tau'_{kl}}(\tau'_{kl}) = \mathcal{F}_{\mathbf{v}'}^{-1}\{r_{kl}(\mathbf{v}')\}$ [38, Sec. 7.3]. Hence, the PDP can be expressed as

$$S_{\tau'_{kl}}(\tau'_{kl}) = \int_{-\infty}^{\infty} r_{kl}(\mathbf{v}') e^{j2\pi \mathbf{v}' \tau'_{kl}} d\mathbf{v}'. \quad (\text{D.62})$$

From the PDP $S_{\tau'_{kl}}(\tau'_{kl})$, we can derive two other important characteristic quantities, namely the *average delay* and the *delay spread*. The average delay is denoted by

$B_{\tau'_{kl}}^{(1)}$ and defined as the first moment of the PDP $S_{\tau'_{kl}}(\tau'_{kl})$, i.e.,

$$B_{\tau'_{kl}}^{(1)} = \frac{\int_0^{\infty} \tau'_{kl} S_{\tau'_{kl}}(\tau'_{kl}) d\tau'_{kl}}{\int_0^{\infty} S_{\tau'_{kl}}(\tau'_{kl}) d\tau'_{kl}}. \quad (\text{D.63})$$

The delay spread is denoted by $B_{\tau'_{kl}}^{(2)}$ and defined by the square root of the second central moment of $S_{\tau'_{kl}}(\tau'_{kl})$, i.e.,

$$B_{\tau'_{kl}}^{(2)} = \sqrt{\frac{\int_0^{\infty} (\tau'_{kl} - B_{\tau'_{kl}}^{(1)})^2 S_{\tau'_{kl}}(\tau'_{kl}) d\tau'_{kl}}{\int_0^{\infty} S_{\tau'_{kl}}(\tau'_{kl}) d\tau'_{kl}}}. \quad (\text{D.64})$$

Alternatively, the equivalent expressions for $B_{\tau'_{kl}}^{(1)}$ and $B_{\tau'_{kl}}^{(2)}$ can be obtained by using Fourier transform techniques, which allows us to present the average delay $B_{\tau'_{kl}}^{(1)}$ and the delay spread $B_{\tau'_{kl}}^{(2)}$ in terms of the FCF $r_{kl}(v')$ as well as its first and second frequency derivative at the origin as [38, p. 64]

$$B_{\tau'_{kl}}^{(1)} = \frac{1}{2\pi j} \cdot \frac{\dot{r}_{kl}(0)}{r_{kl}(0)} \quad (\text{D.65})$$

and

$$B_{\tau'_{kl}}^{(2)} = \frac{1}{2\pi} \sqrt{\left(\frac{\dot{r}_{kl}(0)}{r_{kl}(0)}\right)^2 - \frac{\ddot{r}_{kl}(0)}{r_{kl}(0)}}. \quad (\text{D.66})$$

It is worth mentioning that owing to the inequality $\max\{\delta_T, \delta_R\} \ll R$, both the average delay $B_{\tau'_{kl}}^{(1)}$ and the delay spread $B_{\tau'_{kl}}^{(2)}$ can be independent of k and l .

V. SIMULATION MODEL

Here, we describe the simulation model and we provide some background information on the parametrization methods usually used to determine the parameters of the simulation model. Furthermore, we also present a measurement-oriented method for the computation of the model parameters.

A. Description of the Simulation Model

The reference model presented in Section III is an analytical model, which assumes an infinite number of scatterers ($M, N \rightarrow \infty$). Owing to the practical imple-

mentation complexity, the reference model is non-realizable. However, the reference model described in Section III can serve as a starting point for the derivation of stochastic and deterministic simulation models. Using the generalized principle of deterministic channel modelling [38, Sec. 8.1], a stochastic simulation model can be obtained from the reference model described by (D.2) by using only a finite number of scatterers. By employing this concept, an accurate and efficient channel simulator can be designed, which allows us to reproduce the statistical properties of the reference model with high accuracy controlled by M and N . Several different models are available that can be used for the simulation of mobile radio channels. Here, we have used an SOC model, which allows the efficient modelling and simulation of mobile radio channels under realistic nonisotropic scattering conditions. A detailed description of SOC models can be found in [42] and [43]. In the literature, several parametrization techniques for SOC models have been proposed, such as the extended method of exact Doppler spread (EMEDS) [6], the LPNM [42], and the generalized method of equal areas (GMEA) [44]. In our proposed model, we computed the model parameters by using the LPNM, which is one of the best parameter computation methods for the design of SOC channel simulators.

B. The Measurement-Based Computation of the Model Parameters

In this section, we determine the set of model parameters $\mathcal{P} = \{R, x_T, y_T, z_T, x_R, y_R, z_R, c_R\}$ describing the SCT scattering model in such a way that the Doppler spread $B_f^{(2)}$ and the delay spread $B_{\tau_{kl}}^{(2)}$ of the reference model in (D.61) and (D.66) match the corresponding Doppler spread $B_f^{\star(2)}$ and delay spread $B_{\tau_{kl}}^{\star(2)}$ of the measured channel, respectively. To find the set of model parameters \mathcal{P} , we minimize the error function

$$E_{\min} = W_1 E_1 + W_2 E_2 \quad (\text{D.67})$$

where W_1 and W_2 denote the weighting factors. The symbols E_1 and E_2 in (D.67) stand for the absolute errors of the Doppler spread and the delay spread, respectively, which are defined as

$$E_1 = \arg \min_{\mathcal{P}} \left| B_f^{\star(2)} - B_f^{(2)} \right| \quad (\text{D.68})$$

$$E_2 = \arg \min_{\mathcal{P}} \left| B_{\tau_{kl}}^{\star(2)} - B_{\tau_{kl}}^{(2)} \right|. \quad (\text{D.69})$$

In (D.68) and (D.69), the notation $\arg \min_x f(x)$ denotes the set of elements that achieve the global minimum of $f(x)$. At the beginning of the optimization proce-

ture, the weighting factors W_1 and W_2 are selected such that they satisfy the equality $W_1 + W_2 = 1$. There is a scarcity of measured channels with respect to both delay statistics and the Doppler statistics in tunnel environments. Therefore, we use only the delay spread of the measured channel reported in [36]. Thus, we have set the weighting factor W_1 to zero, implying that the error function E_{\min} in (D.67) equals $E_{\min} = E_2$.

By using the measured channel in [36], we have computed the measurement-based model parameters under two different scenarios, called Scenarios I and II. Scenarios I and II stand for the cases where the transmitter antenna height z_T^* is set to 8 and 2.5 m, respectively, while the receiver antenna height z_R^* equals 2.5 m for both cases. For Scenario I, two points were used for the mobile receiver MS_R in the x -axis, i.e., $x_R^* = \{25, 50\}$. However, for Scenario II, we have considered only one point for MS_R in the x -axis, where MS_T and MS_R were separated from each other by 50 m, i.e., $x_R^* = 50$. For the computation of the model parameters, we have considered 200 scatterers (ciscoids), i.e., $M \times N = 10 \times 20$. For the measured channels in [36], the measured delay spreads $B_{\tau_{kl}}^{*(2)}$ are presented for two different scenarios in Table D.1. In the same table, we have also presented the resulting optimized model parameters and the corresponding delay spreads $B_{\tau_{kl}}^{(2)}$. From the results found for the simulation model, we observe an excellent fitting of delay spreads of the simulation model to those of the measured channel, which proves the validity of the proposed SCT scattering C2C channel simulator. It is worth mentioning that not only the delay spreads but also the transmitter and receiver antenna heights closely agree with those used in the measured equipment (see Table D.1).

VII. NUMERICAL RESULTS

Here, we present numerical results obtained by evaluating (D.52)–(D.55) and (D.66). The correctness of the analytical results will be verified by simulations. The performance of the tunnel channel simulator has been assessed by comparing the temporal ACF and the FCF with the corresponding correlation functions of the reference model described by (D.54) and (D.55), respectively.

As our geometrical scattering model, we consider a SCT with a radius of $R = 5$ m and a length of $L = 100$ m. With reference to Fig. D.3, the locations of the transmitter and the receiver are defined by the Cartesian coordinates $(x_T, y_T, z_T) = (20 \text{ m}, 2 \text{ m}, 1 \text{ m})$ and $(x_R, y_R, z_R) = (40 \text{ m}, 2 \text{ m}, 1 \text{ m})$, respectively. For the reference model, all numerical results have been obtained by choosing the following parameters: $\varphi_V^T = \varphi_V^R = 0^\circ$, $\phi_T = \phi_R = 45^\circ$, $\gamma_T = \gamma_R = 45^\circ$, and $f_{T_{\max}} = f_{R_{\max}} = 91$ Hz.

Table D.1: Measurement-based parameters of the SCT scattering model and the resulting delay spread.

SCT model parameters	Scenario I		Scenario II
	$z_T^* = 8$ m		$z_T^* = 2.5$ m
	$z_R^* = 2.5$ m [36]		$z_R^* = 2.5$ m [36]
	$x_R^* = 25$ m	$x_R^* = 50$ m	$x_R^* = 50$ m
R (m)	9.87	6.83	7.14
x_T (m)	0.01	0.01	0.012
y_T (m)	0.01	0.01	0.01
z_T (m)	8.2	7.9	2.57
x_R (m)	22.4	54.66	53.9
y_R (m)	0.01	0.01	0.01
z_R (m)	2.7	2.64	2.62
c_R	0.5	0.51	0.52
Measured delay spread $B_{\tau_{kl}}^{*(2)}$ (ns) [36]	10	5	5
Theoretical delay spread $B_{\tau_{kl}}^{(2)}$ (ns)	10	5	5

In [20], it is stated that the LOS component may contain more than just the true LOS signal, for example, the ground specular component. In our numerical studies, for the sake of simplicity, we do not take into account the effect of the specular component, i.e., c_R^{SPE} is set to zero. Thus, the Rice factor c_R equals $c_R = c_R^{\text{LOS}} + c_R^{\text{SPE}} = c_R^{\text{LOS}}$, which was chosen from the set $\{0, 0.5, 1\}$. The effective scatterers are randomly distributed on the SCT wall over a length of $x_R - x_T = 20$ m. The LPNM has been used to optimize the parameters of the simulation model by assuming a finite number of scatterers (cisoids). For the simulation model, the number of scatterers was set to $M \times N = 30 \times 20$.

The absolute value of the 2D space CCF $|\rho_{11,22}(\delta_T, \delta_R)|$ of the reference model has been computed by using (D.52). The obtained results are illustrated in Fig. D.4 for an NLOS ($c_R = 0$) propagation scenario. We can observe that the 2D space CCF $|\rho_{11,22}(\delta_T, \delta_R)|$ decreases as the antenna element spacings δ_T and δ_R increase. For comparison reasons, the absolute value of the 2D space CCF is depicted in

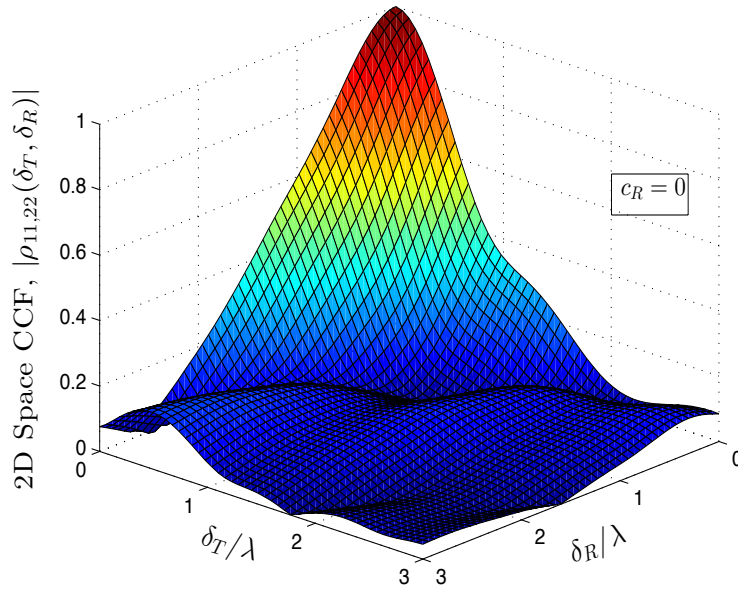


Figure D.4: Absolute value of the 2D space CCF $|\rho_{11,22}(\delta_T, \delta_R)|$ of the reference model for an NLOS propagation scenario ($c_R = 0$).

Fig. D.5 for a LOS ($c_R = 1$) propagation scenario. As can be seen in Fig. D.5, under LOS propagation conditions, the TVTFs $H(f', t)$ and $H(f' + v', t + \tau)$ are highly correlated even for relatively large antenna element spacings.

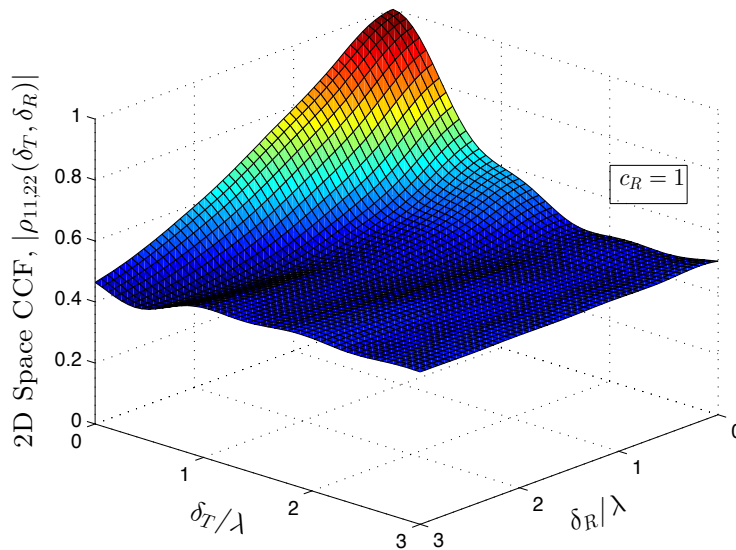


Figure D.5: Absolute value of the 2D space CCF $|\rho_{11,22}(\delta_T, \delta_R)|$ of the reference model for a LOS propagation scenario ($c_R = 1$).

Similarly, the absolute value of the 2D TF-CCF $|\rho_{11}(v', \tau)|$ of the reference model has been evaluated by using (D.53). Figs. D.6 and D.7 illustrate the results

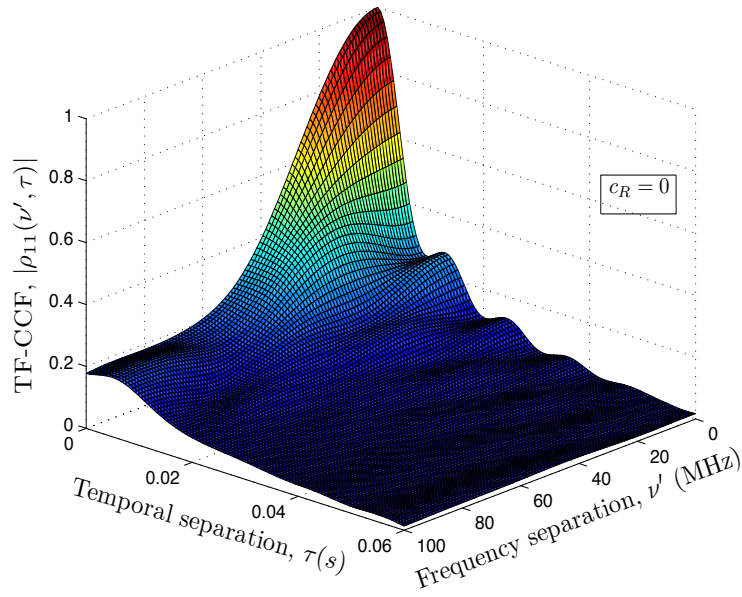


Figure D.6: Absolute value of the 2D TF-CCF $|\rho_{11}(\nu', \tau)|$ of the reference model for an NLOS propagation scenario ($c_R = 0$).

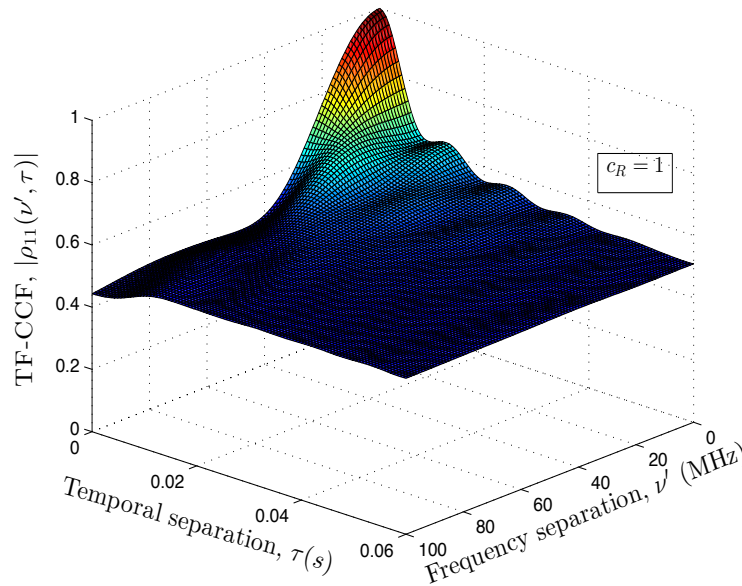


Figure D.7: Absolute value of the 2D TF-CCF $|\rho_{11}(\nu', \tau)|$ of the reference model for a LOS propagation scenario ($c_R = 1$).

for NLOS ($c_R = 0$) and LOS propagation scenarios. Regarding the influence of a LOS component, the 2D TF-CCF $|\rho_{11}(\nu', \tau)|$ behaves similar as the 2D space CCF.

Fig. D.8 shows the absolute value of the temporal ACF $|r_{kl}(\tau)|$ for the case that the transmitter and the receiver are moving with the same speed in the same direction. A good match between the temporal ACF of the reference model and the

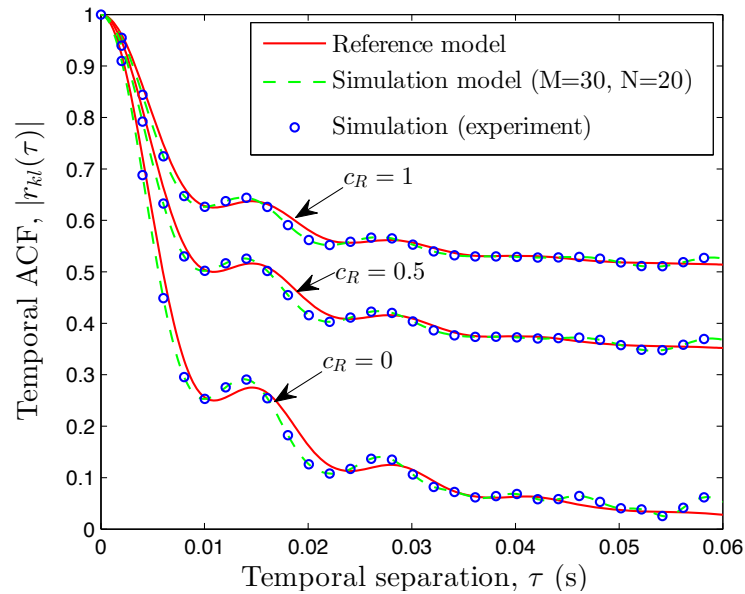


Figure D.8: Absolute value of the temporal ACF $|r_{kl}(\tau)|$ of the reference model and the temporal ACF of the simulation model for different Rice factors c_R .

simulation model can be observed. Fig. D.8 demonstrates also that the experimental simulation results of the temporal ACF match very well with the theoretical results. The experimental results have been obtained by computing the time average of the deterministic SCT simulation model making use of MATLAB function *xcorr.m*.

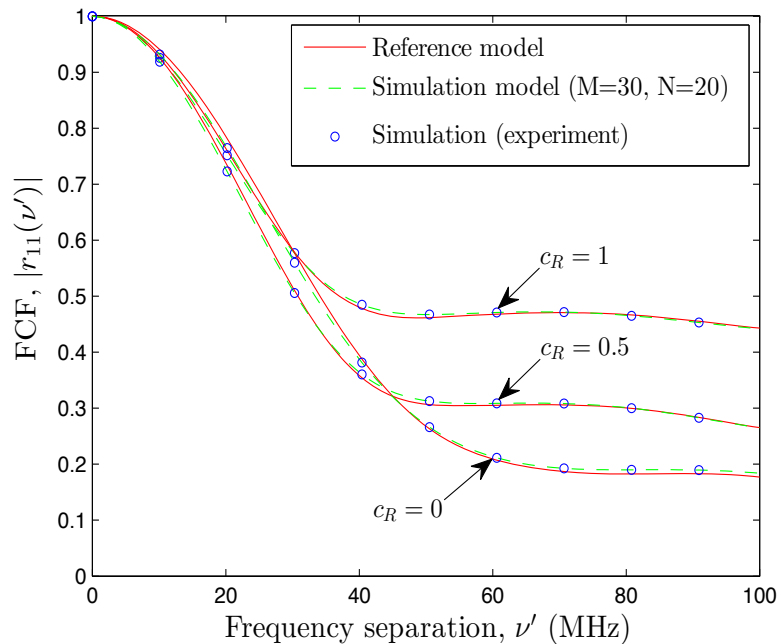


Figure D.9: Absolute value of the FCF $|r_{11}(\nu')|$ of the reference model and the FCF of the simulation model for different Rice factors c_R .

Fig. D.9 shows the absolute value of the FCF $|r_{11}(\nu')|$ for the same scenario. A good agreement between the FCF of the reference model and the simulation model can be seen. Again, it can be observed that the experimental simulation results of the FCF match very well with the theoretical ones. From Fig. D.9, we can conclude that our proposed SCT scattering model can be considered as a frequency-nonselctive channel model for dedicated short-range communications (DSRC) systems [14], where the system bandwidth is 10 MHz. In both Figs. D.8 and D.9, we can observe that the approximation errors caused by a limited number of scatterers (cisoids) M and N can in general be neglected in the presented domains of τ and ν' if $M \geq 30$ and $N \geq 20$.

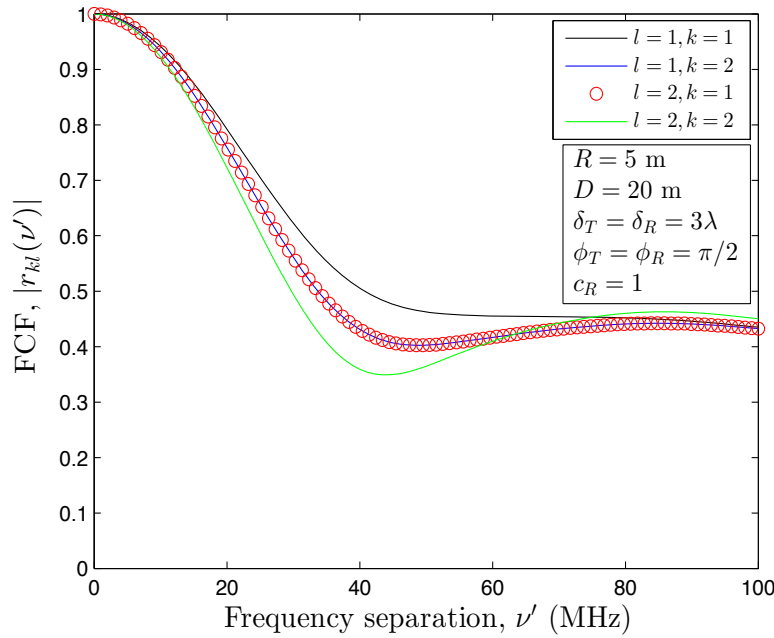


Figure D.10: Absolute value of the FCF $|r_{kl}(\nu')|$ of the reference model for different transmission links $A_T^{(l)} - A_R^{(k)}$ ($l, k = 1, 2$) under LOS propagation conditions ($c_R = 1$).

In Fig. D.10, the absolute value of the FCF $|r_{kl}(\nu')|$ is shown for different transmission links $A_T^{(l)} - A_R^{(k)}$ ($l, k = 1, 2$) under LOS propagation conditions. It is interesting to see that the FCF $|r_{kl}(\nu')|$ has the same curves for the transmission links $A_T^{(1)} - A_R^{(2)}$ and $A_T^{(2)} - A_R^{(1)}$, which shows the symmetrical positions of the mobile transmitter and the mobile receiver.

Figures D.11 and D.12 present the delay spread $B_{\tau_{kl}}^{(2)}$ evaluated by using (D.66) for different values of the SCT arch radius R under NLOS and LOS propagation conditions, respectively. By increasing the tunnel arch radius R from 5 to 8 m, we can observe that the delay spread increases. By comparing Figs. D.11 and D.12,

we can see that the delay spread under LOS propagation conditions is smaller than the one under NLOS conditions. This fact can be attributed to the presence of a strong direct path.

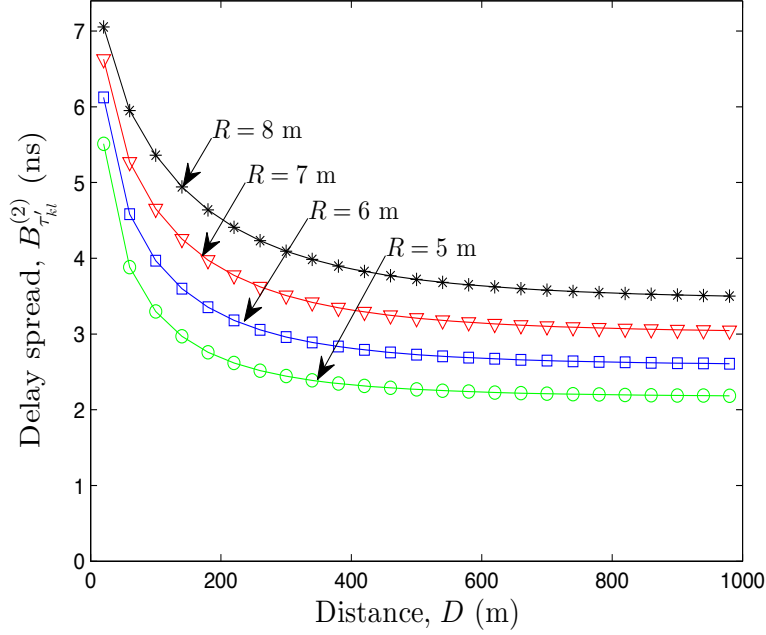


Figure D.11: Delay spread $B_{\tau_{kl}}^{(2)}$ of the reference model for different values of the radius R of the tunnel arch under NLOS propagation conditions ($c_R = 0$).

Figure D.13 shows the delay spread $B_{\tau_{kl}}^{(2)}$ for different transmission links from $A_T^{(l)}$ to $A_R^{(k)}$ under NLOS propagation conditions, where the transmitter (receiver) antenna element spacing δ_T (δ_R) is in the order of the tunnel radius R , such as $\delta_T = \delta_R = 3\lambda$. Similarly to Fig. D.10, from Fig. D.13 it can be observed that the delay spread $B_{\tau_{kl}}^{(2)}$ has identical graphs for the transmission links $A_T^{(1)} - A_R^{(2)}$ and $A_T^{(2)} - A_R^{(1)}$, which attributes to the symmetrical positions of the mobile transmitter and the mobile receiver. For comparison reasons, in Fig. D.14, we present the delay spreads $B_{\tau_{kl}}^{(2)}$ for small values of δ_T and δ_R , i.e., $\delta_T = \delta_R = 0.3\lambda$. One can see that the delay spreads $B_{\tau_{kl}}^{(2)}$ are the same for all transmission links from $A_T^{(l)}$ to $A_R^{(k)}$ ($l, k = 1, 2$), which means that the delay spread $B_{\tau_{kl}}^{(2)}$ can be considered as independent of l and k if the inequality $\max\{\delta_T, \delta_R\} \ll R$ holds.

VIII. CONCLUSION

In this paper, a reference model for a wideband MIMO C2C channel has been derived by starting from the geometrical SCT scattering model. In this model, it has been assumed that the scatterers are randomly distributed on the wall of an

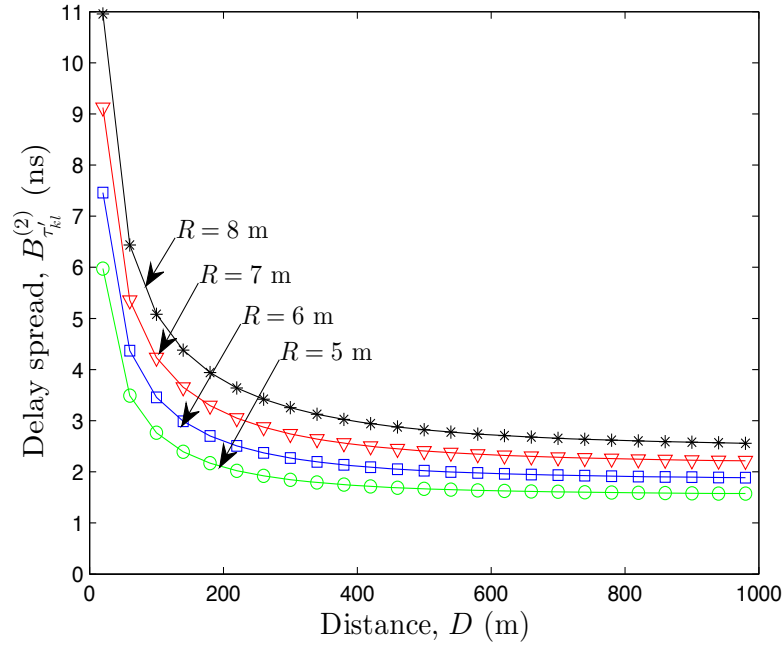


Figure D.12: Delay spread $B_{\tau_{kl}}^{(2)}$ of the reference model for different values of the radius R of the tunnel arch under LOS propagation conditions ($c_R = 1$).

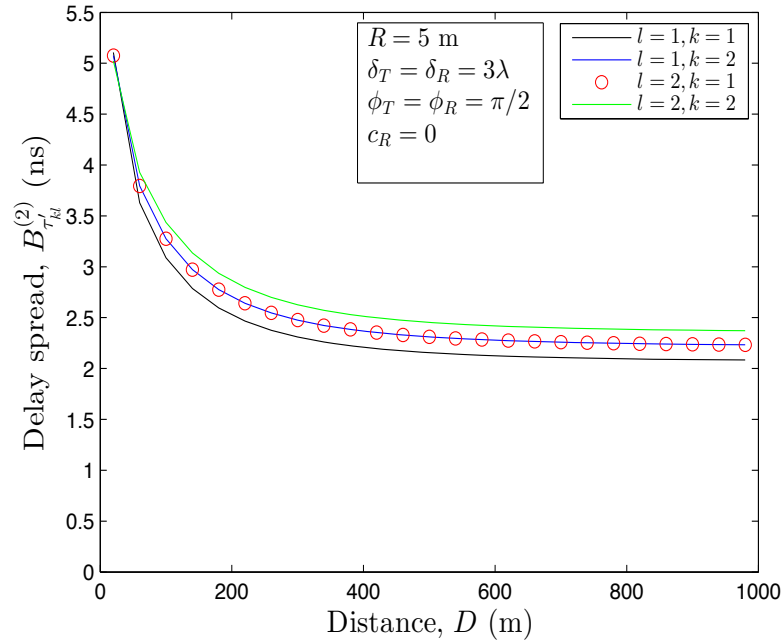


Figure D.13: Delay spread $B_{\tau_{kl}}^{(2)}$ of the reference model for different transmission links from $A_T^{(l)}$ to $A_R^{(k)}$ ($l, k = 1, 2$) under NLOS propagation conditions ($c_R = 0$), if $\delta_T = \delta_R = 3\lambda$.

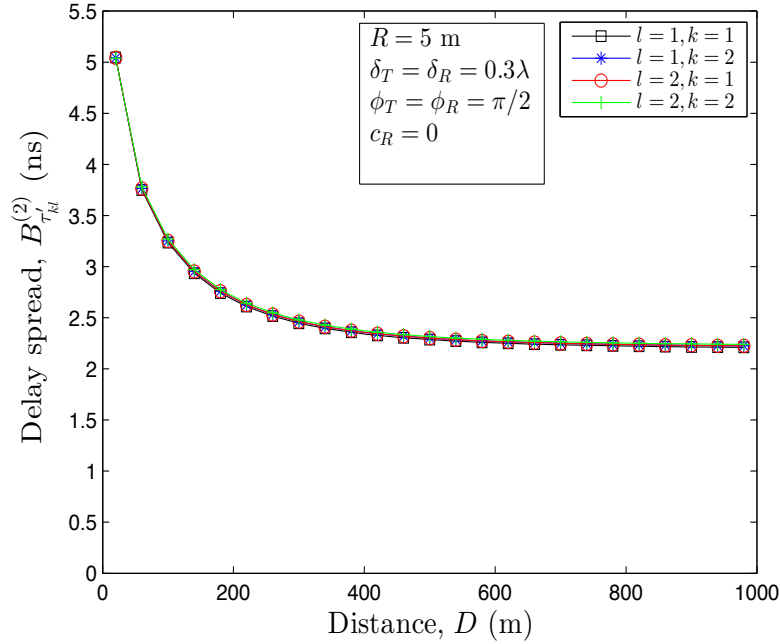


Figure D.14: Delay spread $B_{\tau_{kl}}^{(2)}$ of the reference model for different transmission links from $A_T^{(l)}$ to $A_R^{(k)}$ ($l, k = 1, 2$) under NLOS propagation conditions ($c_R = 0$), if $\delta_T = \delta_R = 0.3\lambda$.

SCT. Taking into account single-bounce scattering under LOS and NLOS propagation conditions, we have analyzed the STF-CCF of the reference model. To find a proper simulation model, the SOC principle has been applied. It has been shown that the designed SOC channel simulator approximates closely the reference model with respect to the temporal ACF and the FCF. Moreover, the delay spread of the reference channel model has been evaluated and presented for both LOS and NLOS propagation environments. A validation of the usefulness of the proposed model has been done by demonstrating an excellent fitting of the delay spreads of the reference model to those of measured channels. Validating the proposed channel model with respect to the other channel statistical quantities could be a topic for future studies, if the required measured data is available. Numerical results have shown that the proposed model can be considered as a narrowband model for DSRC systems, where the system bandwidth is 10 MHz. The proposed channel model allows us to study the effect of multipath propagation on the performance of future C2C communication systems under propagation conditions, which are typical for tunnels.

REFERENCES

- [1] G. Rafiq, B. Talha, M. Pätzold, J. G. Luis, G. Ripa, I. Carreras, C. Coviello, S. Marzorati, G. P. Rodrigues, G. Herrero, and M. Desaeger, “What’s new in intelligent transportation systems? An overview of European projects and initiatives,” *IEEE Veh. Technol. Mag.*, vol. 8, no. 4, pp. 45–69, Dec. 2013.
- [2] Car-to-Car Communication Consortium (C2C-CC) [Online]. Available: <http://www.car-to-car.org>.
- [3] European Road Transport Telematics Implementation Coordinating Organization (ERTICO) [Online]. Available: <http://www.ertico.com>.
- [4] Intelligent Transportation Systems (ITS) [Online]. Available: <http://www.its.dot.gov>.
- [5] G. Bansal and J. B. Kenney, “Controlling congestion in safety-message transmissions: a philosophy for vehicular DSRC systems,” *IEEE Veh. Technol. Mag.*, vol. 8, no. 4, pp. 20–26, Dec. 2013.
- [6] M. Pätzold, B. O. Hogstad, and N. Youssef, “Modeling, analysis, and simulation of MIMO mobile-to-mobile fading channels,” *IEEE Trans. Wireless Commun.*, vol. 7, no. 2, pp. 510–520, Feb. 2008.
- [7] M. Pätzold and B. O. Hogstad, “A wideband MIMO channel model derived from the geometrical elliptical scattering model,” *Wireless Communications and Mobile Computing*, vol. 8, pp. 597–605, May 2008.
- [8] N. Avazov and M. Pätzold, “Design of wideband MIMO car-to-car channel models based on the geometrical street scattering model,” *Special Issue: Modeling and Simulation in Engineering*, vol. 2012, Sept. 2012.
- [9] H. Zhiyi, C. Wei, Z. Wei, M. Pätzold, and A. Chelli, “Modelling of MIMO vehicle-to-vehicle fading channels in T-junction scattering environments,” in *Proc. 3rd European Conference on Antennas and Propagation, EuCAP 2009*. Berlin, Germany, Mar. 2009, pp. 652–656.
- [10] A. Theodorakopoulos, P. Papaioannou, T. Abbas, and F. Tufvesson, “A geometry based stochastic model for MIMO V2V channel simulation in cross-junction scenario,” in *Proc. 13th International Conference on ITS Telecommunications*. Tampere, Finland, Nov. 2013.

- [11] N. Avazov and M. Pätzold, “A novel MIMO car-to-car channel model based on the geometrical curved street scattering model,” in *Proc. Loughborough Antennas and Propagation Conference (LAPC’2012)*, Loughborough, UK, Nov. 2012, pp. 1–6.
- [12] L. Cheng, B. E. Henty, D. D. Stancil, F. Bai, and P. Mudalige, “Mobile vehicle-to-vehicle narrow-band channel measurement and characterization of the 5.9 GHz dedicated short range communication (DSRC) frequency band,” *IEEE J. Select. Areas Commun.*, vol. 25, no. 8, pp. 1501–1516, Oct. 2007.
- [13] X. Cheng, C.-X. Wang, D. I. Laurenson, S. Salous, and A. V. Vasilakos, “An adaptive geometry-based stochastic model for non-isotropic MIMO mobile-to-mobile channels,” *IEEE Trans. Wireless Commun.*, vol. 8, no. 9, pp. 4824–4835, Sept. 2009.
- [14] J. B. Kenney, “Dedicated short-range communications (DSRC) standards in the United States,” *Proceedings of the IEEE*, vol. 99, no. 7, pp. 1162–1182, July 2011.
- [15] A. G. Zajić, G. L. Stüber, T. G. Pratt, and S. T. Nguyen, “Wideband MIMO mobile-to-mobile channels: geometry-based statistical modeling with experimental verification,” *IEEE Trans. Veh. Technol.*, vol. 58, no. 2, pp. 517–534, Feb. 2009.
- [16] Y. Yuan, X. Cheng, C.-X. Wang, D. I. Laurenson, X. Ge, and F. Zhao, “Space-time correlation properties of a 3D two-sphere model for non-isotropic MIMO mobile-to-mobile channels,” in *Proc. of the IEEE Global Telecommunications Conference (GLOBECOM’10)*, Dec 2010, pp. 1–5.
- [17] J. Chen and T. G. Pratt, “A three-dimensional geometry-based statistical model of 2×2 dual-polarized MIMO mobile-to-mobile wideband channels,” *Modelling and Simulation in Engineering*, vol. 2012, Article ID 756508, 2012.
- [18] T. Abbas, L. Bernado, A. Thiel, C. Mecklenbräuker, and F. Tufvesson, “Radio channel properties for vehicular communication: merging lanes versus urban intersections,” *IEEE Veh. Technol. Mag.*, vol. 8, no. 4, pp. 27–34, Dec. 2013.
- [19] O. Renaudin, V.-M. Kolmonen, P. Vainikainen, and C. Oestges, “Wideband measurement-based modeling of inter-vehicle channels in the 5.2 GHz band,” *IEEE Trans. Veh. Technol.*, vol. 62, no. 8, pp. 3531–3540, Oct. 2013.

- [20] J. Karedal, F. Tufvesson, N. Czink, A. Paier, C. Dumard, T. Zemen, and C. F. Mecklenbräuker, “A geometry-based stochastic MIMO model for vehicle-to-vehicle communications,” *IEEE Trans. Wireless Commun.*, vol. 8, no. 7, pp. 3646–3657, July 2009.
- [21] J. Maurer, T. Fügen, and W. Wiesbeck, “Narrow-band measurement and analysis of the inter-vehicle transmission channel at 5.2 GHz,” in *Proc. IEEE 55th Semiannual Veh. Technol. Conf., VTC’02-Spring*, vol. 3. Birmingham, Alabama, May 2002, pp. 1274–1278.
- [22] G. Acosta, K. Tokuda, and M. A. Ingram, “Measured joint Doppler-delay power profiles for vehicle-to-vehicle communications at 2.4 GHz,” in *Proc. IEEE Global Communications Conference, GLOBECOM’04, Dallas, TX*, vol. 6, Nov. 29 - Dec. 3 2004, pp. 3813–3817.
- [23] J. Kunisch and J. Pamp, “Wideband car-to-car radio channel measurements and model at 5.9 GHz,” in *2008 IEEE 68th Vehicular Technology Conference*, Calgary, Canada, Sep. 2008, pp. 1–5.
- [24] Y. Ma and M. Pätzold, “Performance analysis of Alamouti coded OFDM systems over Rayleigh fading channels correlated in space and time,” in *Proc. the 71st IEEE Vehicular Technology Conference, VTC2010-Spring, Taipei*, May 2010, pp. 1–6.
- [25] N. Avazov and M. Pätzold, “Performance analysis of Alamouti coded OFDM systems over wideband MIMO car-to-car channels correlated in time and space,” in *Proc. International conference on Connected Vehicles and Expo (ICCVE’2014), Vienna, Austria*, Nov. 2014.
- [26] L. Bernadó, A. Roma, A. Paier, T. Zemen, N. Czink, J. Karedal, A. Thiel, F. Tufvesson, A. F. Molisch, and C. F. Mecklenbräuker, “In-tunnel vehicular radio channel characterization,” in *Proc. 73rd IEEE Vehicular Technology Conference (VTC2011-Spring)*, May 2011, pp. 1–5.
- [27] D. Umansky and M. Pätzold, “Stationarity test for wireless communication channels,” in *Proc. IEEE Global Communications Conference (GLOBECOM’2009), Honolulu, Hawaii, USA*, Nov. 2009.
- [28] X. Cheng, Q. Yao, M. Wen, C.-X. Wang, L.-Y. Song, and B.-L. Jiao, “Wideband channel modeling and intercarrier interference cancellation for vehicle-to-vehicle communication systems,” *IEEE J. Select. Areas Commun.*, vol. 31, no. 9, pp. 434–448, Sept. 2013.

- [29] *Norwegian Public Road Administration, Road Tunnels*. NPRA Printing Center, Apr. 2004.
- [30] S. F. Mahmoud and J. R. Wait, "Geometrical optical approach for electromagnetic wave propagation in rectangular mine tunnels," *Radio Science*, vol. 9, no. 12, pp. 1147–1158, Dec. 1974.
- [31] D. G. Dudley, M. Liénard, S. F. Mahmoud, and P. Degauque, "Wireless propagation in tunnels," *IEEE Antennas Propagation Mag.*, vol. 49, no. 2, pp. 11–26, Apr. 2007.
- [32] K. Arshad, F. Katsriku, and A. Lasebae, "Modelling obstructions in straight and curved rectangular tunnels by finite element approach," *Journal of Electrical Engineering*, vol. 59, no. 1, pp. 9–13, 2008.
- [33] Z. Sun and I. F. Akyildiz, "A mode-based approach for channel modeling in underground tunnels under the impact of vehicular traffic flow," *IEEE Trans. Wireless Commun.*, vol. 10, no. 10, pp. 3222–3231, Oct. 2011.
- [34] T.-S. Wang and C.-F. Yang, "Simulations and measurements of wave propagations in curved road tunnels for signals from GSM base stations," *IEEE Trans. Antennas Propag.*, vol. 54, no. 9, pp. 2577–2584, Sept. 2006.
- [35] S. Hairoud, P. Combeau, Y. Pousset, Y. Cocheril, and M. Berbineau, "WINNER model for subway tunnel at 5.8 GHz," Nov. 2012, pp. 743–747.
- [36] G. S. Ching, M. Ghorraishi, M. Landmann, N. Lertsirisopon, J. i. Takada, T. Imai, I. Samedá, and H. Sakamoto, "Wideband polarimetric directional propagation channel analysis inside an arched tunnel," *IEEE Trans. Antennas Propag.*, vol. 57, no. 3, pp. 760–767, March 2009.
- [37] N. Avazov and M. Pätzold, "A wideband car-to-car channel model based on a geometrical semicircular tunnel scattering model," in *Proc. 24th IEEE Int. Symp. on Personal, Indoor and Mobile Radio Communications (PIMRC'2013), London, UK*, Sept. 2013, pp. 248–253.
- [38] M. Pätzold, *Mobile Radio Channels*, 2nd ed. Chichester: John Wiley & Sons, 2011, 583 pages.
- [39] M. Pätzold, A. Szczepanski, and N. Youssef, "Methods for modeling of specified and measured multipath power-delay profiles," *IEEE Trans. Veh. Technol.*, vol. 51, no. 5, pp. 978–988, 2002.

- [40] A. G. Zajić, G. L. Stüber, T. G. Pratt, and S. Nguyen, “Statistical modeling and experimental verification of wideband MIMO mobile-to-mobile channels in highway environments,” in *Proc. IEEE 19th International Symposium on Personal, Indoor and Mobile Radio Communications, PIMRC 2008*, Sept. 2008, pp. 1–5.
- [41] A. Papoulis and S. U. Pillai, *Probability, Random Variables and Stochastic Processes*, 4th ed. New York: McGraw-Hill, 2002.
- [42] M. Pätzold and B. Talha, “On the statistical properties of sum-of-cisoids-based mobile radio channel simulators,” in *Proc. 10th International Symposium on Wireless Personal Multimedia Communications, WPMC 2007*. Jaipur, India, Dec. 2007, pp. 394–400.
- [43] C. A. Gutiérrez and M. Pätzold, “The design of sum-of-cisoids Rayleigh fading channel simulators assuming non-isotropic scattering conditions,” *IEEE Trans. Wireless Commun.*, vol. 9, no. 4, pp. 1308–1314, Apr. 2010.
- [44] ———, “The generalized method of equal areas for the design of sum-of-sinusoids simulators for mobile Rayleigh fading channels with arbitrary Doppler spectra,” *Wireless Communications and Mobile Computing*, 2011, doi:10.1002/wcm.1154.